Materials Advances

ROYAL SOCIETY OF CHEMISTRY

PAPER

View Article Online
View Journal | View Issue

Check for updates

Cite this: *Mater. Adv.*, 2025, **6**, 4522

Synergistic Ce/Ag/N-doped ZnO–MWCNT nanocomposites for efficient photocatalytic wastewater remediation with visible light†

Manisha Dagar,[a] Suresh Kumar,[a] Amit Jain,*[b] Anil Vohra,[a] Manohar Singh,[c]
Jasvir Dalal, *[d] Sanjeev Kumar[e] and Sandeep Kaushal [f]

Received 21st March 2025,
Accepted 29th May 2025

DOI: 10.1039/d5ma00258c

rsc.li/materials-advances

This study reports an approach for enhancing the photocatalytic efficiency of ZnO by co-doping with cerium (Ce), silver (Ag), and nitrogen (N), supported by multi-walled carbon nanotubes (MWCNTs). The Ce/Ag/N-doped ZnO–MWCNT nanocomposites were synthesized *via* a hydrothermal method, resulting in a significant reduction in the band gap from 3.19 eV to 2.89 eV. This change enabled higher visible light absorption, achieving enhanced photocatalytic degradation efficiencies of 92.12% for Congo red and 87.5% for methylene blue within 80 minutes. Comprehensive characterization using XRD, FTIR, BET, and PL analyses revealed enhanced surface area, increased oxygen vacancies, and improved charge separation dynamics due to the synergistic effects of multi-element doping and MWCNT integration. The strategic incorporation of Ce, Ag, and N not only reduced the electron–hole recombination rate but also facilitated the generation of reactive oxygen species (ROS) that are crucial for efficient dye degradation. These findings indicate the significant potential of the synthesized nanocomposites as advanced photocatalysts for environmental remediation under visible light irradiation.

1. Introduction

Recent advances in photocatalysis have focused on the synthesis of zinc oxide (ZnO) nanostructures, which possess the ability to respond to visible light. These ZnO nanostructures have been synthesized using various methods, including co-doping with metals and the development of nanocomposites, which have garnered significant research attention.[1–3] The combination of ZnO with metals such as silver (Ag) and other metal oxides has been extensively studied to enhance its photocatalytic activity.[4,5] This exploration has deepened the understanding of how doping affects the electronic and structural properties of ZnO, leading to improved photocatalytic efficiency. The development of nanocomposites has paved the way for synthesizing hybrid nanostructures with superior photocatalytic properties. A promising strategy in the design of ZnO-based nanocomposites involves incorporating carbon nanotubes (CNTs), which play a crucial role in enhancing photocatalytic performance.[6] CNTs, owing to their exceptional electrical conductivity, high surface area, and mechanical strength, serve as efficient charge carriers that reduce electron–hole recombination. By facilitating charge separation, CNTs improve the photocatalytic activity of semiconductor materials like ZnO. Moreover, the large surface area provided by CNTs offers more active sites for catalytic reactions, further boosting the degradation of pollutants. The integration of ZnO with CNTs not only enhances electron transport but also stabilizes the structure, making CNT-based nanocomposites highly effective in wastewater treatment.[7]

ZnO nanostructures can be synthesized in a variety of morphologies, including nanoparticles (nps), nanowires, and nanosheets that can be synthesized using hydrothermal techniques, which offer precise control over the physical and chemical properties. This tunability is crucial for optimizing the photocatalytic performance of ZnO-based materials, especially for environmental applications like pollutant degradation and water purification.[8] The need for clean and affordable water remains one of the most critical global challenges. Although water covers approximately 71% of the Earth's surface, only about 3% is freshwater, much of which is unevenly

---

[a] *Department of Electronic Science, Kurukshetra University, Kurukshetra-136119, India*
[b] *Department of Electronics, Rajdhani College, University of Delhi, Delhi-110015, India. E-mail: amitjainudsc@gmail.com*
[c] *Department of Physics, Motilal Nehru College, University of Delhi, Delhi-110021, India*
[d] *Department of Physics, Rajdhani College, University of Delhi, Delhi-110015, India. E-mail: jasvirdalal2012@gmail.com*
[e] *Department of Physics, Chandigarh University, Gharuan, Mohali, 140413, India*
[f] *Regional Institute of Education, NCERT, Ajmer, Rajasthan, India*

† Electronic supplementary information (ESI) available. See DOI: **https://doi.org/10.1039/d5ma00258c**

distributed and increasingly contaminated by human activities.[9] This exacerbates the issue of water scarcity, highlighting the urgent need for sustainable solutions. In this context, the development of ZnO-based nanostructures represents a promising approach for water purification and environmental remediation, as these materials have shown considerable potential in breaking down harmful pollutants.[10]

Recent research has focused on enhancing the photocatalytic efficiency of ZnO-based nanocomposites, particularly for wastewater treatment applications. Advanced doping strategies involving both metals and non-metals have been employed to modify the bandgap energy of ZnO, improving its visible light absorption and reducing electron–hole recombination. Metals such as Au, Ni, Pt, Mg, Fe, Cr, Ce, and Gd, alongside non-metals like F, S, B, N, Si, and C, have been used to narrow the bandgap and promote efficient charge separation, thereby enhancing photocatalytic activity.[11–14] Furthermore, the development of ZnO-doped nanocomposites with mesoporous architectures has increased the surface area available for catalytic reactions, further improving photocatalytic performance. These innovations represent significant progress in photocatalytic technologies aimed at pollutant degradation. The unique properties of CNTs make them ideal scaffolds for ZnO nanostructures, facilitating efficient electron transfer, improving stability, and increasing surface area for reactions.[15] The studies reveal that ZnO/CNT nanocomposites have shown significant promise in environmental applications, particularly in enhancing photocatalytic properties.[16] Modifications to the bandgap and crystal structure of photocatalysts have been shown to improve their performance significantly.

In this study, we investigated the effects of incorporating cerium (Ce), nitrogen (N), and silver (Ag) dopants into ZnO-lined CNTs. The hydrothermal method was employed due to its ability to control particle morphology and size. The photocatalytic efficacy of the resulting nanocomposites was evaluated through degradation of methylene blue and Congo red dyes under visible light, assessing their potential for environmental applications.

2. Experimental details

2.1. Chemicals used

The following high-purity reagents of analytical grade were used for the synthesis of Ag/Ce/N-doped ZnO–CNT nanocomposites. Sodium hydroxide pellets (NaOH), zinc nitrate hexahydrate ($Zn(NO_3)_2·6H_2O$), *tert*-butanol (*t*-BuOH), *p*-benzoquinone (*p*-BQ), ammonium oxalate (AO), and potassium persulfate ($K_2S_2O_2$) were procured from Merck. Urea (CH_4N_2O), silver nitrate ($AgNO_3$), Congo red dye ($C_{32}H_{22}N_6Na_2O_6S_2$), multi-walled carbon nanotubes (MWCNTs), and cerium nitrate hexahydrate ($Ce(NO_3)_3·6H_2O$) were procured from Sigma-Aldrich. All chemicals were utilized as received without further purification.

2.2. Synthesis of Ag/Ce/N-doped ZnO–MWCNT nanocomposites

The synthesis of Ag/Ce/N-doped ZnO–MWCNT nanocomposites was conducted in a series of designed steps, supported by specific chemical reactions to ensure the formation of the desired nanocomposite. First, zinc nitrate hexahydrate is dissolved in water, providing the zinc precursor, which dissociates as follows:

$$Zn(NO_3)_2·6H_2O \rightarrow Zn^{2+} + 2NO_3^{-} + 6H_2O$$

The zinc ions (Zn^{2+}) serve as the precursor for ZnO formation during hydrothermal processing. MWCNTs are dispersed in this solution *via* ultrasonication, creating a homogeneous suspension. Silver nitrate, cerium nitrate hexahydrate, and urea were dissolved in deionized water.

Silver nitrate dissociates into silver ions;

$$AgNO_3 \rightarrow Ag^{+} + NO_3^{-}$$

Cerium nitrate dissociates into cerium ions;

$$Ce(NO_3)_3·6H_2O \rightarrow Ce^{3+} + 3NO_3^{-} + 6H_2O$$

Urea acts as the nitrogen source, and under hydrothermal conditions, it undergoes hydrolysis, producing ammonia and carbon dioxide, which contributes to nitrogen doping;

$$CH_4N_2O + H_2O \rightarrow 2NH_3 + CO_2$$

Sodium hydroxide is dissolved in water to create hydroxide ions, which serves as a reducing agent. The hydroxide ions (OH^{-}) promote the formation of ZnO from Zn^{2+} ions;

$$Zn^{2+} + 2OH^{-} \rightarrow Zn(OH)_2$$

Upon heating during the hydrothermal treatment, zinc hydroxide ($Zn(OH)_2$) dehydrates to form zinc oxide (ZnO);

$$Zn(OH)_2 + \text{Heat} \rightarrow ZnO + H_2O$$

During the hydrothermal process at 85 °C, zinc ions (Zn^{2+}) from zinc nitrate react with hydroxide ions (OH^{-}) from sodium hydroxide to form zinc hydroxide ($Zn(OH)_2$), which then dehydrates to form ZnO nps. These ZnO nps nucleate and grow on the MWCNTs' surface, creating a composite structure. Simultaneously, silver (Ag), cerium (Ce), and nitrogen (N) are doped into the ZnO lattice, enhancing its photocatalytic properties. The reactions can be presented as follows:

Formation of $Zn(OH)_2$:

$$Zn^{2+} + 2OH^{-} \rightarrow Zn(OH)_2$$

Dehydration of $Zn(OH)_2$ to form ZnO:

$$Zn(OH)_2 + \text{Heat} \rightarrow ZnO + H_2O$$

The ZnO nps nucleate and grow on the MWCNT surface due to their high surface area, allowing for enhanced interaction between the nanomaterial and the MWCNT scaffold;

$$ZnO(\text{nps}) \rightarrow ZnO@MWCNT$$

Co-doping of ZnO on MWCNTs: during the hydrothermal process, the dopants Ag^{+}, Ce^{3+}, and N^{3-} are simultaneously introduced into the ZnO lattice, forming a co-doped structure. These ions either substitute Zn^{2+} in the lattice or occupy interstitial sites, while nitrogen (from the hydrolysis of urea)

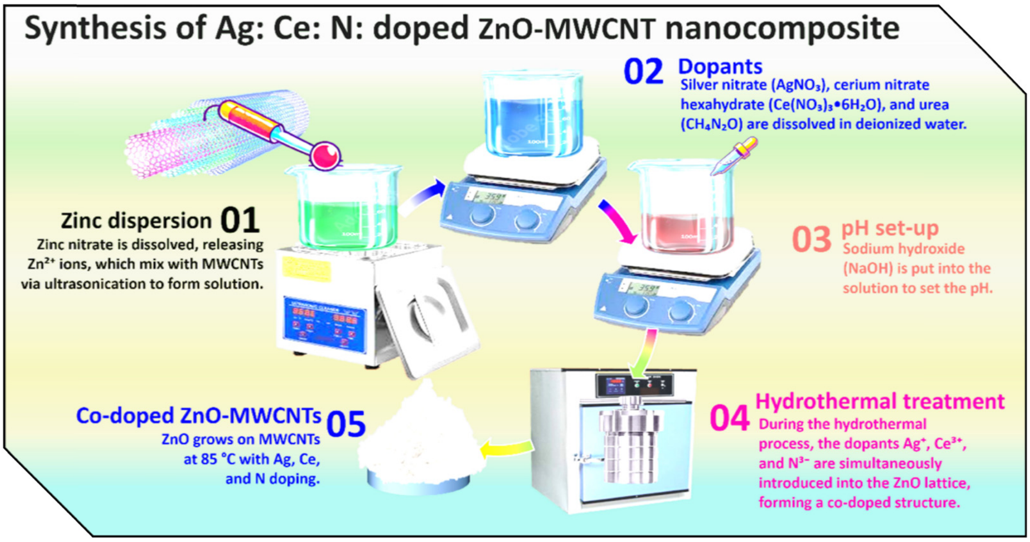

Fig. 1 Schematic representation of the hydrothermal synthesis process for Ce/Ag/N-doped ZnO–MWCNT nanocomposites.

is also incorporated as a dopant. The overall co-doping reaction on MWCNTs can be represented as:

$$\mathrm{ZnO@MWCNT} + \mathrm{Ag}^{+} + \mathrm{Ce}^{3+} + \mathrm{N}^{3-} \rightarrow \text{Ag/Ce/N-co-doped ZnO@MWCNT}$$

The MWCNTs backing the composite also enhance the electron transport pathways, contributing to the overall improvement in photocatalytic activity. After hydrothermal processing, the co-doped ZnO nps are well-dispersed on the surface of the MWCNTs, forming the final Ag/Ce/N-co-doped ZnO–MWCNT nanocomposite. A schematic of the complete synthesis process is presented in Fig. 1.

To explore the effect of varying cerium concentrations on the photocatalytic performance of Ag/Ce/N-doped ZnO–MWCNT nanocomposites, four distinct samples were synthesized. These samples were labelled based on their cerium content as tabulated in Table 1. In samples N3–N4, the N and Ag concentrations were kept constant at 2% each, serving to augment trap levels and enhance charge separation efficiency in the photocatalytic process.

2.3 Photocatalytic activity measurement

Photocatalytic degradation experiments were conducted following a systematic procedure, as shown in Fig. S1 (ESI†). Initially, a dye solution of Congo red was prepared by dissolving the dye in 150 mL of distilled water. To this solution, a precise quantity of 0.05 grams of the synthesized Ce/Ag/N-doped ZnO–MWCNT photocatalyst was introduced, resulting in what is referred to as solution 1. This solution was carefully prepared to maintain controlled dye concentrations, ensuring reproducibility and accuracy in the experimental outcomes.

Table 1 Chemical composition of the synthesized Ce/Ag/N-doped ZnO–MWCNT nanocomposites, detailing the variations in Ce doping concentration while maintaining Ag and N levels constant

Sample code	Chemical composition
N1	Pure ZnO
N2	ZnO (94%) + Ce (2%) + Ag (2%) + N (2%) + 0.1 g CNT
N3	ZnO (92%) + Ce (4%) + Ag (2%) + N (2%) + 0.1 g CNT
N4	ZnO (90%) + Ce (6%) + Ag (2%) + N (2%) + 0.1 g CNT

Then, solution 1 was followed by sonication to achieve a homogeneous distribution of the photocatalyst within the solution. To facilitate the initial adsorption of the dye onto the photocatalyst surface, the mixture was allowed to stand in darkness for 90 minutes. This step was critical for maximizing the adsorption of Congo red onto the photocatalyst, which is known to enhance the overall photocatalytic efficiency. Once the adsorption period concluded, the photocatalytic degradation was initiated by placing the solution on a magnetic stirrer. The photocatalyst was activated under a phosphor-coated mercury vapor lamp emitting light in the wavelength range of 400–550 nm, thereby simulating visible light conditions that promote photocatalytic reactions. During the experiment, 15 mL samples were systematically withdrawn at 15-minute intervals. Each sample was immediately filtered and centrifuged to eliminate any suspended solids, ensuring that only the dissolved dye concentration was measured. The quantitative assessment of dye concentration reduction was performed using UV-visible spectrophotometry. The photocatalytic degradation efficiency of organic dyes was determined using the following equation.[17]

$$\text{Degradation efficiency }(\%) = \frac{A_0 - A_t}{A_0} \times 100 \qquad (1)$$

where A_0 represents the initial concentration of methyl orange, and A_t denotes the concentration of methyl orange at time t. This equation quantifies the percentage of organic dye degradation during the photocatalytic process. This methodology was followed for a precise evaluation of the photocatalyst's performance while minimizing environmental impact. The experimental design not only ensures the reliability of the results but also provides insights into the kinetics and mechanisms underlying the photocatalytic degradation process.

3 Results & discussion

3.1 Structural analysis

The X-ray diffraction (XRD) patterns of the Ag/Ce/N-doped ZnO–MWCNT nanocomposites were recorded over a 2θ range of 20° to 80° (Fig. 2). The characteristic peaks at 31.74°, 34.21°, 36.20°, 47.43°, 56.48°, 62.81°, and 67.83° are assigned to the (100), (002), (101), (102), (110), (103), and (112) planes of the hexagonal wurtzite ZnO structure, as per JCPDS card no. 80-0075. The retention of these peaks confirms the preservation of the wurtzite phase of ZnO, even after co-doping and the integration of MWCNTs. In addition to the wurtzite ZnO peaks, secondary peaks at 27.90°, 38.15°, and 64.40° correspond to the (110), (111), and (220) planes of Ag_2O_3 (JCPDS cards 30-0443 and 84-1108), while a peak at 28.41° indicates the presence of cerium oxide (Ce^{3+}) phases (JCPDS card no. 75-0392). The sharp peak at 26.31° is associated with the (002) plane of MWCNTs, signifying the successful incorporation of the carbon framework into the composite. The detection of these secondary phases suggests that while some dopant ions may substitute into the ZnO lattice, others form distinct phases, contributing to heterojunction formation within the nanocomposite.

The incorporation of Ce and Ag dopants leads to significant modifications in the XRD diffraction profiles, reflecting alterations in the crystalline structure of ZnO. The gradual increase in the intensity of cerium-related peaks from samples N2 to N4 indicates a progressive integration of Ce^{3+} ions into the ZnO lattice. This integration is accompanied by a noticeable decrease in the intrinsic ZnO peak intensities, suggesting a partial substitution of smaller Zn^{2+} ions (ionic radius = 0.74 Å) with larger Ce^{3+} ions (ionic radius = 1.01 Å).[18] This ionic substitution disrupts the lattice symmetry, inducing localized lattice strain due to the size mismatch. This strain is manifested as a systematic shift of ZnO peaks towards lower 2θ angles, indicating lattice expansion and an increase in interplanar spacing (d-spacing). The resulting lattice distortion promotes the formation of intrinsic point defects, particularly oxygen vacancies (V_o), which act as electron donors, enhancing charge carrier mobility. The broadening of the peaks observed at higher Ce concentrations (N3 and N4) further suggests increased microstrain within the lattice, which could result from the co-existence of multiple dopants with differing ionic radii.[4] The induced strain and defect density are beneficial for photocatalytic processes, as they create additional reactive sites and energy levels within the band structure, facilitating efficient electron excitation under visible light irradiation. These structural modifications through co-doping thus effectively tune the lattice parameters, optimizing the material for enhanced photocatalytic performance.

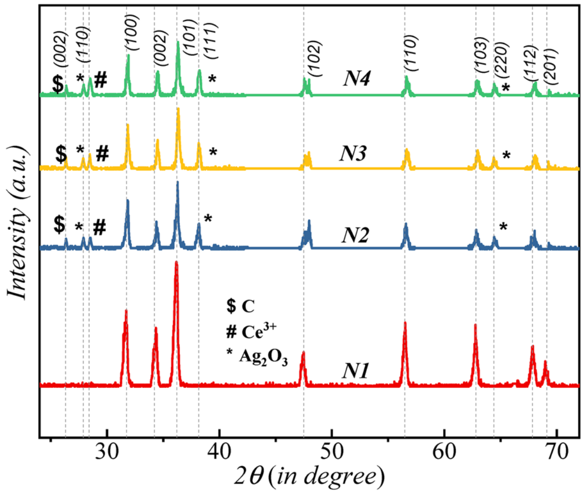

Fig. 2 XRD patterns of Ce/Ag/N-doped ZnO–MWCNT nanocomposites with varying Ce concentrations, confirming phase purity, crystallinity, and the presence of dopants.

Using the Debye–Scherrer equation,[19] the crystallite size was found to increase slightly from 21.5 nm (N1) to 23.8 nm (N4). However, the observed peak broadening in samples N3 and N4 implies a competition between crystallite growth and the introduction of microstrain. The increasing microstrain can be measured using Williamson–Hall analysis, which suggests that higher dopant concentrations induce lattice distortions, thereby increasing defect densities. These defects are beneficial for catalytic applications as they enhance surface reactivity.

The incorporation of MWCNT enhances the stability of the ZnO lattice by providing a robust scaffold. Moreover, the high aspect ratio of MWCNTs can lead to improved stress distribution within the nanocomposite, reducing the impact of lattice strain induced by heavy doping. Furthermore, the presence of Ag and Ce phases suggests heterostructure formation, which may further enhance charge separation by creating localized electric fields at the interfaces. The presence of these heterojunctions, coupled with the lattice distortions caused by nitrogen doping (likely present as interstitials or substitutions), results in the generation of oxygen vacancies. These vacancies are evident from the changes in peak broadening and shifting patterns and are crucial in enhancing the catalytic activity by providing additional reactive sites.

The XRD analysis confirms that the co-doping of ZnO with Ce, Ag, and N, along with the incorporation of MWCNTs, induces significant structural modifications as tabulated in Table 2. The lattice expansion, peak shifts, and broadening provide evidence of strain and defect generation, which are key factors in enhancing the material's catalytic efficiency.

3.2 FTIR spectroscopy analysis

Fourier transform infrared (FTIR) spectroscopy was employed to analyse the functional groups present in the Ag/Ce/N-doped ZnO–MWCNT nanocomposites, as depicted in Fig. 3. The FTIR spectra reveal distinct absorption peaks that are indicative of the successful incorporation of dopants and the presence of functional groups crucial to the nanocomposites' structural and photocatalytic properties. The presence of ZnO is confirmed by prominent absorption bands in the range of 450 to

Table 2 Crystallite size and lattice parameters of the synthesized nanocomposites based on XRD analysis, showing changes in unit cell dimensions and bandgap energy with dopant concentration

Sample name	D (nm)	A (Å)	C (Å)	c/a	Band gap (eV)
N1	21.5	3.268	5.231	1.6006	3.19
N2	21.9	3.255	5.219	1.6033	3.03
N3	23.4	3.244	5.205	1.6045	2.93
N4	23.8	3.250	5.222	1.6067	2.89

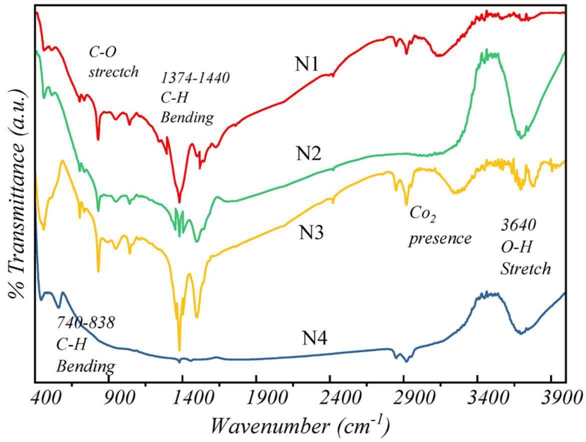

Fig. 3 FTIR spectra of Ce/Ag/N-doped ZnO–MWCNT nanocomposites, showing characteristic vibrational modes corresponding to ZnO, dopant incorporation, and functional groups.

650 cm^{-1}, attributed to Zn–O stretching vibrations, which are essential for the nanocomposite's structural framework.[20] The observed shift in these peaks with increasing cerium content suggests lattice distortion and the successful incorporation of Ce ions, which can enhance defect sites conducive to photocatalytic activity. A broad absorption band centred around 3640 cm^{-1} is assigned to the O–H stretching vibration, indicating the presence of surface hydroxyl groups.[21] These hydroxyl groups are known to act as active sites in photocatalysis, promoting the generation of reactive oxygen species. The increased intensity of this peak with higher Ce content (N3 and N4) suggests enhanced surface hydroxylation, potentially boosting photocatalytic efficiency.

The presence of N–H stretching vibrations is evident in the range of 3210 to 3540 cm^{-1}, which confirms the incorporation of nitrogen into the ZnO lattice.[22] This incorporation is crucial as nitrogen doping is known to introduce localized energy levels within the bandgap, thereby enhancing visible light absorption. Also, the peak identified between 1510 and 1650 cm^{-1} corresponds to the presence of nitro groups (–NO_2),[23] suggesting that nitrogen is effectively integrated into the nanocomposite structure, potentially leading to improved charge separation. The C–H bending vibrations detected at 740 to 838 cm^{-1} and 1374 to 1440 cm^{-1} are attributed to residual organic groups from the carbon nanotubes and other organic precursors used during synthesis. The strong absorption band at 1048 cm^{-1} is assigned to C–O stretching, indicative of the functional groups associated with MWCNTs and the organic capping agents used in the synthesis.[24] This peak also highlights the role of MWCNTs in providing a robust support matrix, improving the dispersion and stability of ZnO nps.

The FTIR spectra show variations in peak intensities and positions as the cerium concentration increases, particularly in the O–H, N–H, and C–O stretching regions. These changes suggest that the introduction of Ce, Ag, and N dopants significantly alters the surface chemistry of ZnO, enhancing its hydrophilicity and reactivity. The co-existence of these functional groups, particularly the increased presence of O–H groups and nitrogen-based functionalities, is likely to enhance the adsorption of pollutant molecules and the subsequent generation of ROS, thereby improving photocatalytic performance.

The incorporation of Ce and Ag, coupled with nitrogen doping, not only influences the crystallographic structure (as confirmed by XRD analysis) but also enhances the surface chemistry, as evidenced by FTIR. The increased presence of functional groups, such as hydroxyl and nitro groups, along with nitrogen doping, contributes to improved charge carrier dynamics. These modifications facilitate efficient electron–hole separation, which is crucial for the photocatalytic degradation of organic pollutants. The FTIR analysis confirms the successful incorporation of Ag, Ce, and N dopants into the ZnO–MWCNT nanocomposite matrix. The presence of key functional groups, such as O–H, N–H, and C–O, indicates that the doping process not only modifies the structural integrity of ZnO but also enhances its photocatalytic properties.

3.3 Surface analysis: Brunauer–Emmett–Teller (BET)

The surface properties of the Ag/Ce/N-doped ZnO–MWCNT nanocomposite (sample N4) were thoroughly investigated using BET analysis to evaluate its porosity and surface characteristics (Fig. 4). The analysis revealed significant mesoporous features, which are critical for optimizing the performance of photocatalytic materials. The type IV isotherm observed in Fig. 4(a) is characteristic of mesoporous materials, exhibiting a pronounced hysteresis loop that confirms the presence of well-defined mesopores. The BET surface area of the N4 sample was determined to be 29 m^2 g^{-1}, with a pore volume of 0.54 cc g^{-1} and an average pore diameter of 4.8 nm, as shown in Fig. 4(b). These mesoporous attributes are essential for enhancing photocatalytic efficiency, as the increased surface area provides more active sites for interaction with pollutant molecules. The interconnected pore network facilitates efficient mass transfer, thereby accelerating the degradation of organic dyes under light irradiation.

The multi-point BET analysis (Fig. 4(c)) yielded a slope of 65.47 and an intercept of 2.702 g^{-1}, resulting in a calculated physical surface area of 31.867 m^2 g^{-1}. The high correlation coefficient (R^2 = 0.9998) indicates a strong linear fit, validating the reliability of the measurements. The slight discrepancy between the surface area values obtained from the single and multi-point analyses can be attributed to surface roughness and the presence of heterogeneously distributed pores. Implications of mesoporosity on photocatalytic performance: the presence of a

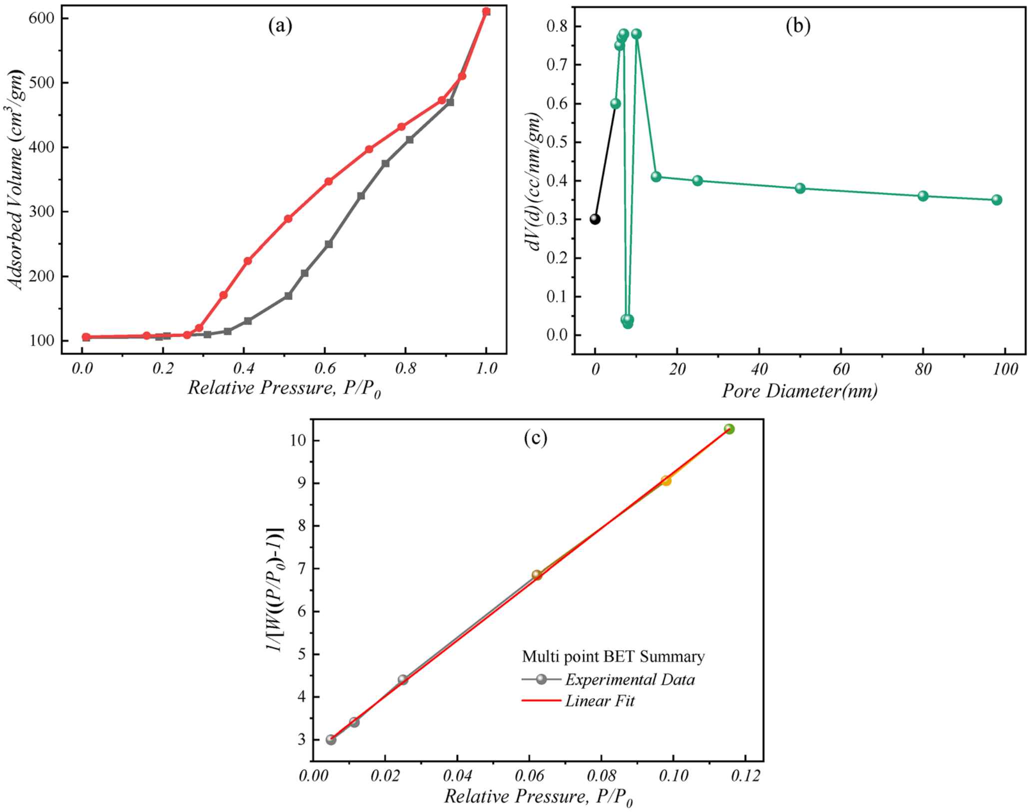

Fig. 4 (a) Nitrogen adsorption–desorption isotherm demonstrating a mesoporous nature; (b) BJH pore size distribution analysis; and (c) multi-point BET analysis confirming increased surface area and porosity of the nanocomposites.

mesoporous structure in the N4 sample enhances the adsorption capacity, enabling efficient uptake of dye molecules and pollutants. The large pore volume and moderate pore size (4.8 nm) ensure effective diffusion of reactants to the active sites, thereby optimizing photocatalytic reactions. Additionally, the increased surface area provided by the integration of MWCNTs within the nanocomposite matrix promotes improved charge separation, reducing electron–hole recombination rates and thus enhancing the overall photocatalytic performance. These analyses highlight the superior mesoporous properties of the Ag/Ce/N-doped ZnO–MWCNT nanocomposite, which contribute to its enhanced photocatalytic capabilities. The synergy between high surface area, optimal pore size distribution, and increased pore volume facilitates efficient interaction with pollutants, indicating the decent photocatalytic characteristics of the composite.

3.4 Morphological studies: FESEM analysis

The morphological characteristics of the Ag/Ce/N-doped ZnO–MWCNT nanocomposite samples (N1 and N4) were analyzed using FESEM, as shown in Fig. 5. The FESEM images reveal significant differences in morphology between the undoped (N1) and heavily doped (N4) samples. The images of the Ce/Ag/N-doped ZnO–MWCNT nanocomposites indicate a uniform dispersion of MWCNTs within the matrix, preventing particle agglomeration and providing an interconnected network for efficient charge transport. The presence of MWCNTs not only stabilizes the ZnO nanostructures but also enhances electron mobility, which is critical for reducing charge recombination and improving photocatalytic activity.

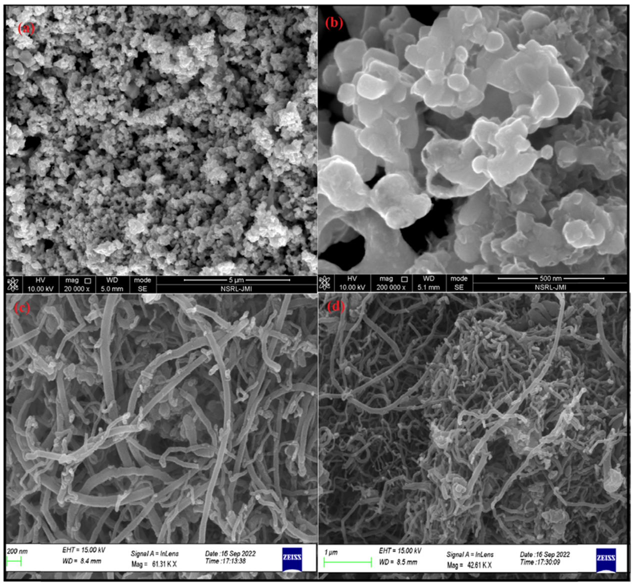

Fig. 5 FESEM images of (a) and (b) undoped ZnO (N1) and (c) and (d) Ce/Ag/N-doped ZnO–MWCNT nanocomposites (N4), showing morphological transformations, and the formation of nanorod-like structures.

Fig. 5(a) and (b) show the morphology of the N1 sample, which consists of densely packed, irregularly shaped nanoplates and aggregated spherical particles. The observed agglomeration is typical in nanomaterials due to high surface energy, leading to reduced surface area and limited access to reactive sites. In contrast, the FESEM images of the co-doped sample N4, shown in Fig. 5(c) and (d), display a more intricate network of interwoven nanorods and nanotubes. The incorporation of Ag, Ce, and N into the ZnO–MWCNT matrix significantly alters the surface morphology, promoting the formation of elongated nanostructures. This transformation is attributed to the role of dopants in modulating nucleation and growth kinetics, resulting in enhanced anisotropic growth. The intertwined nanorod structures observed in N4 suggest a high degree of surface roughness and porosity, which are consistent with the mesoporous characteristics identified in the BET analysis. This mesoporous network facilitates improved mass transport and accessibility of active sites, thereby enhancing the material's catalytic efficiency.

These results are aligned with previous studies on ZnO–carbon nanocomposites, which determine that the strong coupling between ZnO and MWCNTs promotes effective charge separation and enhances photocatalytic efficiency.[25] The high electrical conductivity of MWCNTs facilitates rapid electron transport, minimizing electron–hole recombination and thereby improving the degradation efficiency of organic pollutants.

The compositional analysis of the Ag/Ce/N-doped ZnO–MWCNT nanocomposites (samples N2 and N4) was conducted using energy-dispersive X-ray spectroscopy (EDX), as depicted in Fig. 6. The EDX spectra confirm the successful incorporation of dopants, revealing the presence of key elements, including C, N, O, Zn, Ag, and Ce, uniformly distributed within the ZnO–MWCNT matrix.

The EDX results, supported by quantitative analysis, indicate varying concentrations of dopants between samples N2 and N4. In particular, the elemental weight percentages for sample N2 reveal 2.0 wt% Ag and 1.99 wt% Ce, whereas sample N4 exhibits a higher Ce content of 5.97 wt% and a slightly reduced Ag content of 1.98 wt%. The nitrogen content also increases marginally from 1.99 wt% in N2 to 1.97 wt% in N4, suggesting enhanced incorporation with increased Ce doping. The consistent presence of carbon, albeit in trace amounts, is attributed to the multi-walled carbon nanotube matrix, which acts as a structural support and improves the electronic properties of the composite.

The ability of EDX to map the spatial distribution of elements across the nanocomposite structure provides a crucial understanding of the uniformity of dopant incorporation. This homogeneous distribution of Ag, Ce, and N within the ZnO lattice ensures that the photocatalytic activity is consistent throughout the material. The EDX analysis conclusively determines the successful incorporation and uniform distribution of Ag, Ce, and N dopants within the ZnO–MWCNT nanocomposites. The ability to control the dopant concentrations and their distribution within the matrix provides a pathway to optimizing the material for enhanced photocatalytic activity.

3.5 Optical properties analysis: UV-visible spectroscopy

The optical properties of the Ag/Ce/N-doped ZnO–MWCNT nanocomposites were investigated using UV-visible spectroscopy to evaluate the impact of dopants on the material's electronic structure (Fig. 7). The absorption measurements were performed over a wavelength range of 350 to 700 nm, highlighting a gradual redshift with increasing cerium content. The absorption spectra and Tauc plots reveal significant shifts in the optical band gap as a function of cerium concentration, which are crucial for optimizing photocatalytic efficiency. The optical band gap has been estimated using the following equation;[26]

$$(\alpha h\nu)^{1/n} = A(h\nu - E_g)$$

where α represents the absorption coefficient, h is Planck's constant, n denotes the power factor that depends on the type of electronic transition, and A is a constant. For allowed direct transitions, n is typically set to 1/2. The Tauc's plots (Fig. 7b) have been plotted for precise determination of the optical band gap. The undoped ZnO sample (N1) exhibited a band gap of 3.19 eV, consistent with the intrinsic band gap of bulk ZnO. The absorption spectra of the composites exhibit a redshift in the absorption edge, indicating a reduction in bandgap energy. This shift is attributed to doping-induced modifications in the electronic structure of ZnO, which enhance visible-light absorption and improve photocatalytic efficiency. The calculated bandgap values, obtained from Tauc plot analysis (Fig. 7b), show a progressive reduction from 3.19 eV (undoped ZnO) to 2.89 eV (Ce/Ag/N-doped ZnO), indicating the impact of doping on electronic transitions.

The observed redshift and bandgap narrowing can be attributed to the successful incorporation of Ce, Ag, and N dopants into the ZnO lattice, which induce structural and electronic modifications. Ce^{3+} ions contribute to the formation of oxygen vacancies, generating additional defect states that act as donor levels within the ZnO band structure, facilitating charge carrier mobility and promoting visible light absorption.[27] Ag nanoparticles further influence the optical properties through surface plasmon resonance, extending the absorption range into the visible spectrum. Additionally, nitrogen doping introduces shallow acceptor states, further lowering the bandgap and enabling more efficient utilization of visible light for photocatalysis. These changes are further supported by XRD analysis, which indicates a slight increase in crystallite size with higher doping levels. The increased particle size may reduce quantum confinement effects, contributing to the observed bandgap narrowing. The combination of electronic state modification, structural defects, and improved charge transport pathways collectively enhances the photocatalytic efficiency of the nanocomposites.

The incorporation of Ag, Ce, and N also plays a crucial role in suppressing particle agglomeration and promoting the formation of well-defined nanostructures. Ag nanoparticles serve as nucleation centers, while Ce^{3+} ions influence the crystallization process, promoting anisotropic growth and the

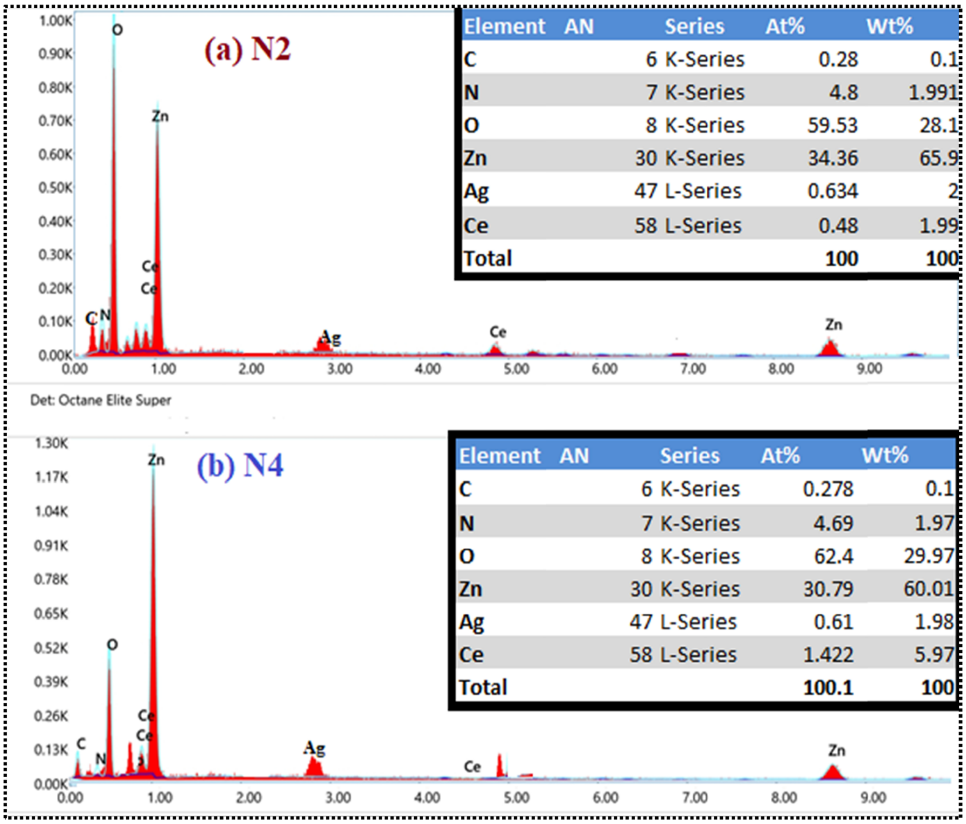

Element	AN	Series	At%	Wt%
C	6	K-Series	0.28	0.1
N	7	K-Series	4.8	1.991
O	8	K-Series	59.53	28.1
Zn	30	K-Series	34.36	65.9
Ag	47	L-Series	0.634	2
Ce	58	L-Series	0.48	1.99
Total			100	100

Element	AN	Series	At%	Wt%
C	6	K-Series	0.278	0.1
N	7	K-Series	4.69	1.97
O	8	K-Series	62.4	29.97
Zn	30	K-Series	30.79	60.01
Ag	47	L-Series	0.61	1.98
Ce	58	L-Series	1.422	5.97
Total			100.1	100

Fig. 6 EDX spectra of the (a) N2 and (b) N4 nanocomposites, confirming the incorporation of Ce, Ag, and N dopants within the ZnO–MWCNT matrix.

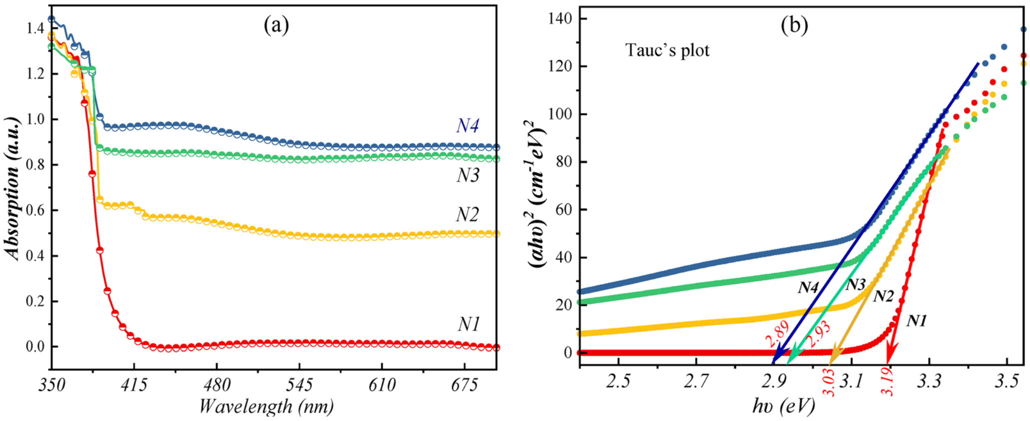

Fig. 7 (a) UV-Vis absorption spectra showing the enhanced light absorption properties of Ce/Ag/N-doped ZnO–MWCNT nanocomposites; (b) Tauc plot indicating bandgap reduction with increasing Ce concentration.

formation of nanorods. Nitrogen doping enhances the formation of surface defects, which contribute to improved charge carrier dynamics, further optimizing the photocatalytic performance. The enhanced surface area and porosity of the doped samples, as confirmed by BET analysis, directly correlate with their superior photocatalytic capabilities. Thus, these results suggest that the synergistic interaction between ZnO and MWCNTs plays a pivotal role in optimizing photocatalytic performance by providing structural stability, enhancing light absorption, and promoting efficient charge carrier dynamics.

3.6 Charge carrier dynamics: photoluminescence (PL) spectroscopy

The PL spectra of the synthesised samples were analysed to evaluate the recombination dynamics of photo-generated charge carriers, as shown in Fig. 8. The PL emission spectra

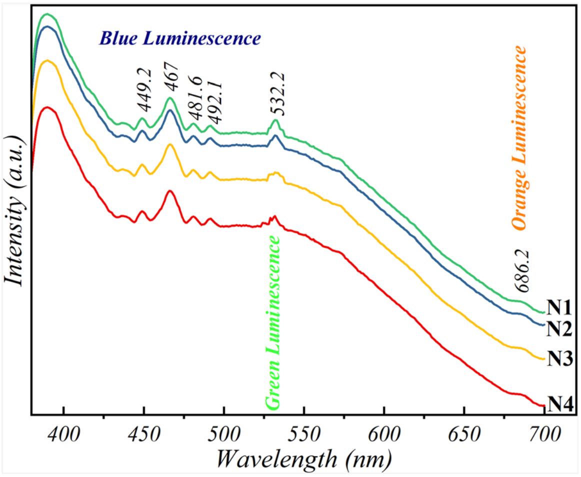

Fig. 8 Photoluminescence spectrum of different nanocomposites, demonstrating reduced emission intensity in doped samples due to suppressed electron–hole recombination, which enhances photocatalytic efficiency.

reveal distinct luminescence peaks in the blue, green, and orange regions, corresponding to various defect states within the ZnO lattice. The PL spectrum of the N1 sample shows strong blue emission peaks at 449.2 nm, 467 nm, and 481.6 nm, which are attributed to near-band-edge (NBE) transitions and intrinsic defects, such as Zn interstitials and oxygen vacancies.[28] The gradual decrease in the intensity of these peaks with increased Ce doping (N2 to N4) indicates a reduction in defect-related recombination pathways. The green luminescence observed at 532.2 nm is commonly associated with singly ionized oxygen vacancies, which act as electron acceptors.[23] The enhancement of this peak in Ce-doped samples suggests an increase in oxygen vacancy concentration, thereby improving the material's ability to generate reactive oxygen species during photocatalysis.

The PL spectra reveal a significant reduction in intensity for the doped samples (N2, N3, N4) compared to the undoped sample, indicating a decrease in the recombination rate of electron–hole pairs, which is critical for enhancing photocatalytic efficiency. The observed quenching of PL intensity is particularly pronounced in the sample with the highest cerium concentration (N4), suggesting that Ce incorporation plays a crucial role in suppressing recombination by introducing additional defect levels within the band structure. Ce^{3+} ions facilitate the creation of localized states within the ZnO bandgap, which act as trap centers for electrons, promoting charge carrier separation.[29] The presence of Ce^{3+} ions enhances the formation of oxygen vacancies and defect states, as evidenced by the green luminescence peak at 532.2 nm. These oxygen vacancies serve as shallow traps, extending the lifetime of photo-generated carriers by preventing their immediate recombination. Moreover, the broad orange luminescence band centered around 686.2 nm in the N4 sample is linked to deep-level defects introduced by Ag and N co-doping.[30] These deep traps contribute to extending the lifetime of charge carriers, thereby increasing the probability of their participation in photocatalytic reactions. The reduction in PL intensity across the doped samples indicates enhanced charge separation efficiency, which is crucial for photocatalytic processes.

The improvement in electron transport due to MWCNT incorporation is primarily attributed to efficient interfacial charge transfer between ZnO and MWCNTs. Upon photoexcitation, ZnO generates electron–hole pairs, where the photogenerated electrons in the conduction band of ZnO are transferred to the MWCNTs due to the favorable band alignment and difference in work function. MWCNTs, possessing high electrical conductivity, serve as electron acceptors and transport channels, effectively reducing recombination losses and prolonging charge carrier lifetime. This enhanced charge separation mechanism is further supported by the observed reduction in PL intensity in the doped nanocomposites, indicating suppressed electron–hole recombination. Furthermore, the synergy between ZnO, MWCNTs, and other dopants elements (Ce, Ag, and N) strengthens the charge transport pathways by introducing defect states that facilitate the migration of charge carriers. This optimized interfacial charge transfer plays a crucial role in enhancing photocatalytic efficiency by ensuring more charge carriers participate in redox reactions, ultimately improving pollutant degradation performance under visible light irradiation.

These findings confirm that co-doping with Ce, Ag, and N significantly modifies the electronic structure of ZnO–MWCNT nanocomposites, reducing recombination rates and enhancing charge carrier mobility. The combined effect of defect engineering, extended charge carrier lifetime, and improved charge transport dynamics reinforces the potential of these materials for photocatalytic applications in environmental remediation.

3.7.1 Photocatalytic degradation analysis. The photocatalytic degradation performance of the synthesised samples was assessed under visible light irradiation using MB and CR as model organic pollutants. The results, as depicted in Fig. 9, reveal significant improvements in photocatalytic activity with increasing concentrations of dopants, particularly cerium. After 80 minutes of visible light exposure, the nanocomposites exhibited marked degradation efficiencies, with N4 indicating the highest performance. For MB, the undoped N1 showed limited degradation capability, achieving only 14.2% degradation after 80 minutes. In contrast, the introduction of dopants led to a substantial enhancement in photocatalytic activity. Specifically, the N2 sample achieved a degradation efficiency of 58.5%. Further improvements were observed with increased cerium content; the N3 sample with 4% Ce demonstrated 76.3% degradation, while the heavily doped N4 sample with 6% Ce achieved an impressive degradation rate of 87.5%. This significant increase in efficiency can be attributed to the role of cerium in enhancing charge carrier separation and facilitating the generation of ROS, which are crucial for the oxidative breakdown of dye molecules. The presence of Ce^{3+} ions introduces additional defect states, such as oxygen vacancies, which act as electron traps, thus reducing the recombination rate of electron–hole pairs and enhancing the photocatalytic performance.[31]

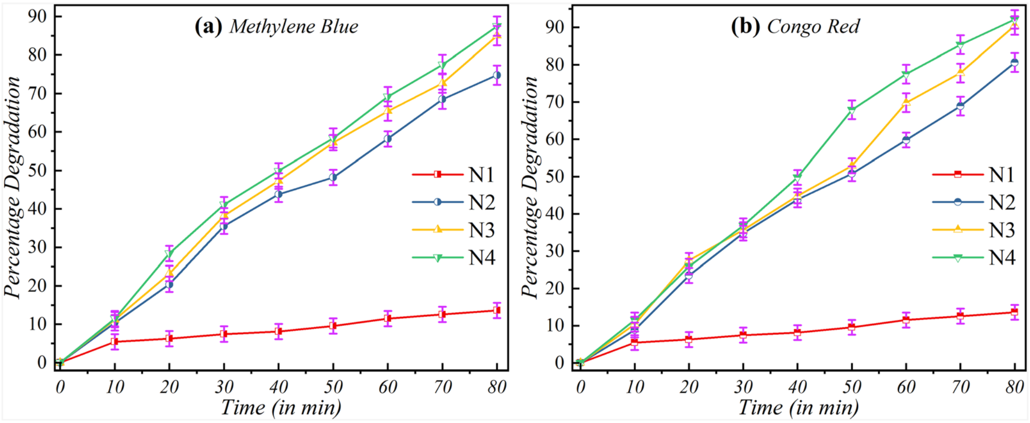

Fig. 9 Photocatalytic degradation efficiency of (a) methylene blue and (b) Congo red under visible light irradiation, showing the enhanced degradation rates of the Ce/Ag/N-doped ZnO–MWCNT nanocomposites compared to undoped ZnO.

Similarly, for CR, the N1 sample displayed minimal activity, achieving only 12.4% degradation after 80 minutes. The incorporation of dopants led to a noticeable increase in degradation efficiency, with the N2 sample reaching 65.2% degradation. The N3 sample exhibited a further improvement with 82.4% degradation, while the N4 sample again showed the best performance, achieving a remarkable degradation rate of 92.12%. The superior photocatalytic performance of N4 is primarily due to the combined effects of Ce, Ag, and N co-doping. The introduction of Ce into the ZnO lattice not only enhances the concentration of oxygen vacancies but also modifies the electronic structure, thereby promoting better charge carrier dynamics. The Ag nps, on the other hand, contribute to surface plasmon resonance, extending light absorption into the visible region and enhancing the generation of photo-excited electrons. Nitrogen doping further aids in narrowing the band gap, making the material more responsive to visible light. The enhanced photocatalytic activity observed in the doped samples, particularly N4, can be attributed to multiple synergistic factors. The structural characterization, supported by BET and PL analyses, confirmed that the co-doping process leads to an increase in surface area, pore volume, and the formation of defect states, which collectively contribute to efficient dye degradation. The mesoporous structure of N4, along with the presence of Ce-induced oxygen vacancies, provides many active sites for dye adsorption and ROS generation. Moreover, the improved charge separation dynamics, facilitated by the presence of Ag nps, significantly reduce the recombination of electron–hole pairs, thereby prolonging the availability of charge carriers for catalytic reactions.

Considering the above discussion, the photocatalytic degradation studies reveal that the Ce/Ag/N-doped ZnO–MWCNT nanocomposites exhibit good performance in degrading organic dyes under visible light irradiation. The enhanced activity, particularly in sample N4, underscores the importance of controlled multi-element doping in optimizing the structural and electronic properties of ZnO nanocomposites.

Furthermore, the long-term stability and recyclability of the photocatalyst are crucial for practical applications. To assess the stability of the synthesized photocatalyst, cyclic degradation tests were performed for MB and CR dyes under the same conditions as shown in Fig. 10. After each cycle, the photocatalyst was recovered, washed with distilled water and ethanol, dried at 80 °C, and reused for subsequent photocatalytic reactions. The degradation efficiencies for MB and CR over four consecutive cycles are as follows: 1st cycle: 87.5% (MB), 92.12% (CR); 2nd cycle: 85.72%, 90.43%; 3rd cycle: 84.3%, 89.25%; 4th cycle: 82.09%, 87.5%. A slight decline in degradation efficiency was observed with successive cycles, which can be attributed to several factors:[32,33] (1) partial blocking of photocatalyst pores by residual dye molecules, reducing adsorption capacity; (2) loss of photocatalyst material during the washing and recovery process; and (3) partial deactivation of active sites due to the accumulation of intermediates from incomplete dye degradation. Despite this minor decrease in activity, the photocatalyst retained a high degradation efficiency after four cycles, indicating good stability and recyclability.

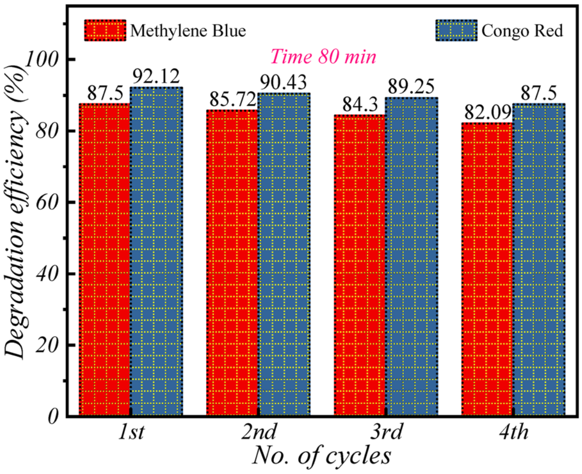

Fig. 10 Catalyst reusability test of Ce/Ag/N-doped ZnO–MWCNT nanocomposites indicating the material's stability and efficiency over multiple reaction cycles.

3.7.2 Kinetic modeling of photocatalytic degradation. The photocatalytic degradation kinetics of Congo red (CR) and methylene blue (MB) dyes using Ce/Ag/N-doped ZnO–MWCNT nanocomposites were analyzed using three kinetic models: pseudo-zero-order, pseudo-first-order, and pseudo-second-order models, as illustrated in Fig. 11 and summarized in Table 3. The study aimed to determine the most suitable kinetic model for describing the degradation process and to evaluate the efficiency of the synthesized photocatalysts.[34]

The pseudo-zero-order kinetic model was first applied to evaluate the degradation rates, as shown in Fig. 11(a). For CR, a degradation rate constant (m_0) of 0.0056 μmol L^{-1} min^{-1} was obtained with a correlation coefficient (R^2) of 0.80. Meanwhile, MB exhibited a rate constant of 0.0053 μmol L^{-1} min^{-1} with an R^2 value of 0.86. These results indicate that while the pseudo-zero-order model captures the initial degradation trends, it may not fully account for the complexities of the photocatalytic process involving multiple reactive intermediates and the formation of ROS. To gain a deeper understanding of the degradation mechanism, the pseudo-first-order model was applied, as shown in Fig. 11(b). The results demonstrate a significantly better fit compared to the zero-order model, with R^2 values of 0.98 for CR and 0.97 for MB. The first-order rate constants (m_1) were found to be 0.0046 min^{-1} for CR and 0.0050 min^{-1} for MB. The high R^2 values indicate that the degradation of both dyes is predominantly governed by first-order kinetics, suggesting that the rate of dye removal is directly proportional to the concentration of the dyes. This behavior aligns with the mechanism of ROS generation, where the availability of reactive sites on the Ce/Ag/N-doped ZnO–MWCNT nanocomposite surface plays a critical role in enhancing degradation efficiency.[35]

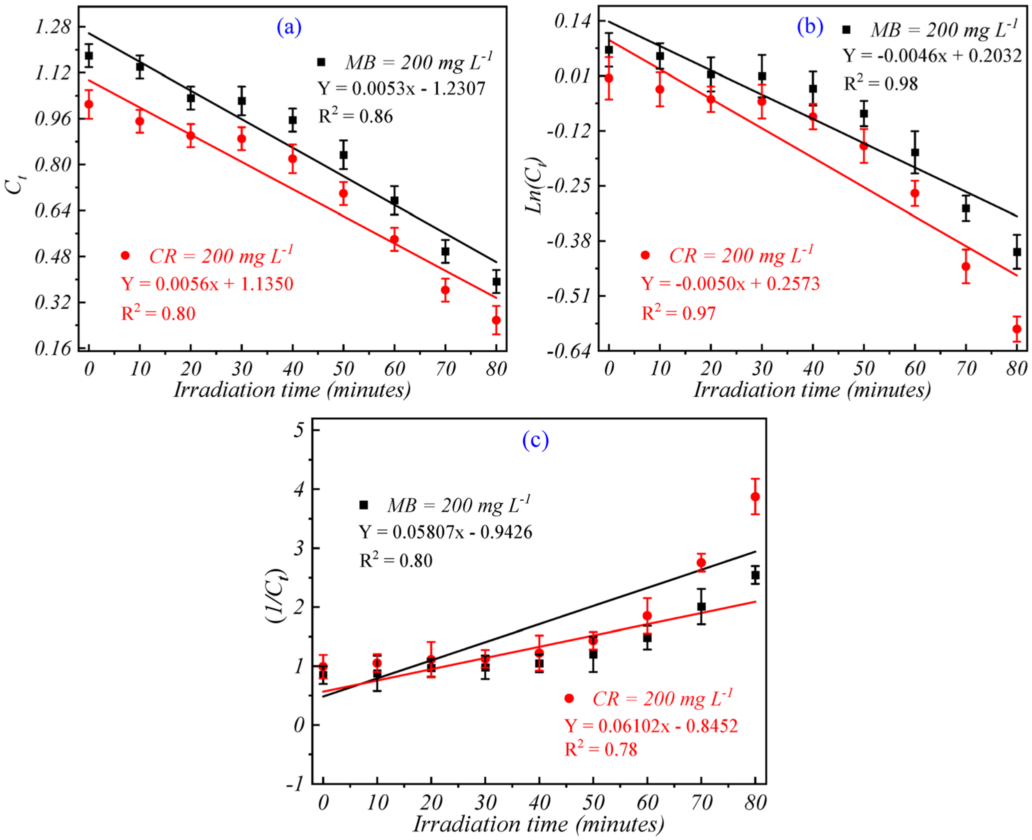

Fig. 11 Kinetic modeling of photocatalytic degradation: (a) pseudo-zero-order, (b) pseudo-first-order, and (c) pseudo-second-order models, showing the reaction kinetics and best-fit model for degradation efficiency.

Table 3 Kinetic parameters for the photocatalytic degradation of Congo Red and Methylene Blue dyes, comparing zero-order, first-order, and second-order models to determine the most suitable reaction mechanism

S. no.	Catalyst dose (mg L^{-1})	% Removal	Zero-order		First-order		Second-order	
			m_0 (μmol L^{-1} min^{-1})	R^2	m_1 (min^{-1})	R^2	m_2 (L μmol min^{-1})	R^2
1	CR = 200	92.12	0.0056	0.80	0.0046	0.98	0.06102	0.78
2	MB = 200	87.50	0.0053	0.86	0.0050	0.97	0.05807	0.80

Further analysis using the pseudo-second-order kinetic model (Fig. 11(c)) yielded rate constants (m_2) of 0.06102 L μmol^{-1} min^{-1} for CR and 0.05807 L μmol^{-1} min^{-1} for MB, with corresponding R^2 values of 0.78 and 0.80, respectively. While the second-order model indicates a reasonable fit, the lower R^2 values compared to the first-order model suggest that the degradation process is not purely controlled by second-order reactions. The higher rate constants for the second-order model suggest strong interactions between dye molecules and the catalyst surface, likely following an adsorption-controlled mechanism. Moreover, the enhanced photocatalytic activity can be attributed to the efficient generation of hydroxyl radicals ($^{\bullet}OH$) and other reactive oxygen species, which facilitate dye degradation. The superior R^2 values obtained for the pseudo-first-order model highlight that the photocatalytic degradation of both CR and MB is most accurately described by first-order kinetics. This indicates that the reaction rate is influenced by the concentration of the dyes and the availability of ROS generated on the surface of the nanocomposites. Thus, the kinetic analysis confirms that the Ce/Ag/N-doped ZnO–MWCNT nanocomposites exhibit outstanding photocatalytic performance, particularly under first-order kinetics, for the degradation of both CR and MB dyes.

3.7.3 Photo-catalytic degradation mechanism. To elucidate the mechanism of photocatalytic degradation, scavenger experiments were performed to identify the dominant reactive oxygen species involved in the photocatalytic process as depicted in Fig. 12. Various scavengers were employed to selectively quench specific reactive species and determine their impact on the degradation efficiency. *tert*-Butanol (*t*-BuOH) was used as a hydroxyl radical ($^{\bullet}OH$) scavenger, *p*-benzoquinone (*p*-BQ) as a superoxide radical ($^{\bullet}O_2^{-}$) scavenger, ammonium oxalate (AO) as a hole (h^+) scavenger, and potassium persulfate ($K_2S_2O_8$) as an electron (e^-) scavenger.[36–39] The degradation efficiency of MB and CR dyes was assessed under different scavenger conditions, revealing a significant reduction in photocatalytic activity when *p*-BQ and *t*-BuOH were introduced. This suggests that superoxide radicals ($^{\bullet}O_2^{-}$) and hydroxyl radicals ($^{\bullet}OH$) play a crucial role in the degradation process. The degradation efficiency decreased marginally in the presence of AO and $K_2S_2O_8$, indicating that photogenerated holes (h^+) and electrons (e^-) contribute to the reaction but are not the primary reactive species.

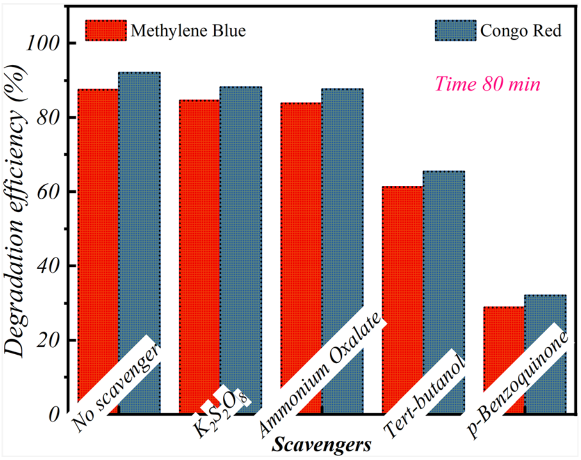

Fig. 12 Photocatalytic degradation of Ce/Ag/N-doped ZnO–MWCNT nanocomposites in the presence of various scavengers, illustrating the role of reactive oxygen species in the photocatalytic degradation process.

The degradation efficiencies for MB and CR in the absence of scavengers were 87.5% and 92.12%, respectively. In contrast, the efficiencies (for MB and CR) dropped significantly upon scavenger addition as, *p*-BQ (28.9% (MB), 32.1% (CR)) < *t*-BuOH (61.3%, 65.4%) < AO (83.8%, 87.7%) < $K_2S_2O_8$ (84.6%, 88.2%). The substantial decline in photocatalytic activity with *p*-BQ confirms that superoxide radicals ($^{\bullet}O_2^{-}$) are the primary contributors to dye degradation. Similarly, the significant reduction observed with *t*-BuOH suggests a major role of hydroxyl radicals ($^{\bullet}OH$) in the reaction mechanism. These results reveal the importance of ROS in the photocatalytic process, indicating that the generation of superoxide and hydroxyl radicals is essential for effective pollutant degradation.[40]

A proposed step-wise photocatalytic degradation mechanism of organic dyes using the Ce/Ag/N-doped ZnO–MWCNT nanocomposites under visible light irradiation is shown in Fig. 13. The enhanced photocatalytic performance is caused by the synergistic process facilitated by multi-element doping and the incorporation of MWCNTs, resulting in efficient charge separation and extended light absorption. Upon exposure to visible light, the Ce/Ag/N-doped ZnO–MWCNT nanocomposites efficiently absorb photons, leveraging their reduced band gap to promote electron excitation. This process generates electron–hole pairs (e^- and h^+) as the photogenerated electrons in the valence band (VB) are excited to the conduction band (CB);

$$\text{Ce/Ag/N-doped ZnO–MWCNT} + h\nu \rightarrow e^-{}_{\text{CB}} + h^+{}_{\text{VB}}$$

The doping of Ce/Ag/N elements in ZnO–MWCNT leads to an increase in the generation of ROS, particularly $^{\bullet}OH$ radicals and $^{\bullet}O_2^{-}$ radicals. The narrowing of the bandgap due to Ce, Ag, and N doping allows more efficient absorption of visible light, leading to enhanced charge carrier generation. Upon photoexcitation, the photogenerated electrons in the conduction band ($e^-{}_{\text{CB}}$) of ZnO react with O_2 to produce $^{\bullet}O_2^{-}$ radicals, while holes in the valence band ($h^+{}_{\text{VB}}$) interact with water molecules or OH^- to generate $^{\bullet}OH$ radicals.[41] The presence of Ce^{3+} ions facilitates the formation of oxygen vacancies, which act as charge carrier traps, reducing recombination and prolonging the lifetime of electrons and holes. These reactions can be presented as;

$$e^-{}_{\text{CB}}\ (\text{Ce/Ag/N-doped ZnO–MWCNT}) + O_2 \rightarrow O_2^{\bullet-}$$

and,

$$h^+{}_{\text{VB}}\ (\text{Ce/Ag/N-doped ZnO–MWCNT}) + H_2O \rightarrow OH^{\bullet} + H^+$$

$$h^+{}_{\text{VB}}\ (\text{Ce/Ag/N-doped ZnO–MWCNT}) + OH^- \rightarrow OH^{\bullet}$$

Moreover, Ag nanoparticles contribute to localized surface plasmon resonance, further enhancing charge carrier separation and improving ROS generation efficiency. Nitrogen doping

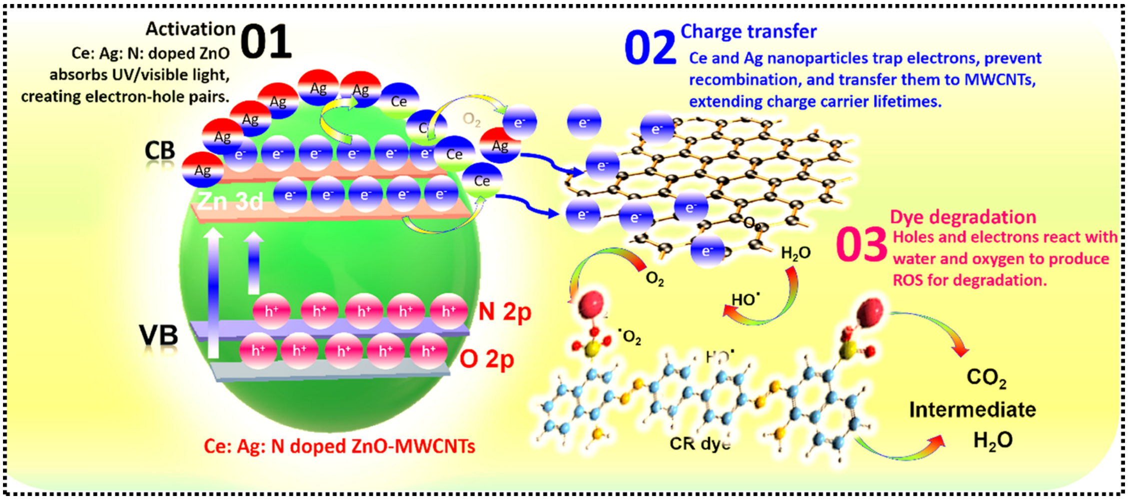

Fig. 13 Proposed photocatalytic mechanism of dye degradation using Ce/Ag/N-doped ZnO–MWCNT nanocomposites, demonstrating charge transfer pathways, reactive oxygen species formation, and pollutant degradation under visible light.

introduces shallow acceptor states, which promote better charge mobility and facilitate redox reactions, increasing the production of $^{\bullet}OH$ and $^{\bullet}O_2^{-}$ radicals. These ROS, specifically $^{\bullet}OH$ radicals and $^{\bullet}O_2^{-}$ radicals, are highly reactive and attack the complex molecular structures of organic dyes like methylene blue and Congo red. This leads to the breakdown of the dye molecules into simpler, non-toxic by-products, which are ultimately mineralized to CO_2 and H_2O;

$$O_2^{\bullet-} + OH^{\bullet} + \text{Dye} \rightarrow \text{non-toxic products} + CO_2 + H_2O$$

The enhanced photocatalytic activity of the Ce/Ag/N-doped ZnO–MWCNT nanocomposites is primarily due to the synergistic effects of multi-element doping combined with the integration of MWCNTs.[42] First, Ce plays a crucial role by increasing the formation of oxygen vacancies, which serve as active sites for the generation of ROS. The redox cycling between Ce^{3+} and Ce^{4+} enhances charge transfer efficiency and extends the lifetime of photogenerated electrons, thereby significantly boosting photocatalytic performance. Secondly, Ag nps act as electron sinks, effectively trapping photogenerated electrons and reducing their recombination with holes. The plasmonic properties of Ag further enhance visible light absorption, increasing the generation of electron–hole pairs under solar irradiation. Meanwhile, N doping modifies the electronic structure of ZnO by introducing intermediate energy levels that reduce the band gap, thus enabling enhanced light absorption in the visible region and promoting the excitation of electrons even under low-energy photons. Moreover, the incorporation of MWCNTs provides a highly conductive matrix that facilitates rapid electron transport, minimizing charge recombination. The high surface area of MWCNTs also improves the adsorption of dye molecules, further enhancing the photocatalytic degradation efficiency of the nanocomposites.

Thus, the Ce, Ag, and N doping, along with MWCNT integration, results in synergy between bandgap narrowing, defect engineering, and enhanced charge separation, which effectively optimizes the photocatalytic efficiency of the nanocomposites. These results provide an understanding of how multi-element doping modulates charge separation and ROS generation, bridging the gap between material properties and observed photocatalytic performance. The incorporation of Ce, Ag, and N strategically enhances visible light absorption and ROS-driven degradation mechanisms, making the synthesized ZnO–MWCNT nanocomposites highly efficient for environmental remediation applications.

3.7.4 Comparison of results with previous work. A comprehensive comparison of the photocatalytic degradation efficiency of the synthesized nanocomposites with previously reported catalysts demonstrates significant advancements, as summarized in Table 4. The comparative analysis underscores the superior performance achieved through strategic doping and the incorporation of multi-walled carbon nanotubes (MWCNTs), which collectively enhance the photocatalytic activity under visible light irradiation.

The highly doped N4 nanocomposites exhibited outstanding photocatalytic efficiencies, achieving 92.12% degradation of Congo red and 87.5% degradation of methylene blue within a notably shorter reaction time of 80 minutes. This is in stark contrast to other doped ZnO systems reported in the literature, where degradation times typically exceed 90 minutes to reach comparable efficiencies. For instance, the N/Ag/ZnO catalyst supported on MWCNTs achieved 98% degradation of MB, but required a longer reaction time of 90 minutes under microwave-assisted hydrothermal conditions, and a Co/N/ZnO nanocomposite reached 78% degradation of CR after 120 minutes, indicating that the extended time required limits its practical applications. The Ce/Ag/N-doped ZnO–MWCNT nanocomposites synthesized in this study not only demonstrated higher degradation rates but also achieved these efficiencies within a reduced timeframe, showcasing their superior catalytic activity. The enhanced performance of the synthesized Ce/Ag/

Table 4 Comparative analysis of the photocatalytic degradation efficiency of Ce/Ag/N-doped ZnO–MWCNT nanocomposites with previously reported catalysts, highlighting the enhanced performance of the synthesized materials

S. no.	Photocatalyst	Methylene blue & Congo red (%)	Time (min)	Process	Ref.
1	Ag-doped ZnO	MB – 95	120	Hydrothermal	43
2	Ce-doped ZnO	MB – 90.7 CR – 90	180	Electrochemical	44
3	Ag-ZnO/Ag_2O	CR – 80	60	Electrochemical	45
4	N-doped ZnO	MB – 83.4	60	Hydrothermal	46
5	ZnO/MWCNT	MB – 50	120	Electrospinning	25
6	Co/N/ZnO	MB – 71 CR – 78	120	P123 + Hydrothermal	47
7	Ag/TiO_2	CR – 61	100	Nano-casting + SBA-15	48
8	In/S/ZnO	MB – 80	90	Hydrothermal + P123	49
9	N/Ag/ZnO	MB – 69 CR – 81	120	EISA + P123	50
10	S/Ni/Ag/ZnO	MB – 67 CR – 79	90	Hydrothermal + F127	51
11	N/Ag/ZnO/MWCNT	MB – 98 CR – 80	90	Hydrothermal + microwave assisted	52
12	Ce/N/Co/ZnO	MB – 79 CR – 93	90	Hydrothermal	53
13	Ce/N/Ag/ZnO/MWCNT	MB – 87.5 CR – 92.12	80	Hydrothermal	This work

N-doped ZnO–MWCNT composites can be attributed to several synergistic factors as discussed in the last section. This approach not only enhances the photocatalytic degradation efficiency but also reduces the time required for complete dye degradation. The superior efficiency and shorter degradation time position the synthesized nanocomposites as promising candidates for environmental remediation applications, particularly in the treatment of wastewater containing hazardous organic dyes.

4. Conclusion

In this study, the photocatalytic activity, stability, and reactive oxygen species ROS generation of a Ce/Ag/N-doped ZnO–MWCNT photocatalyst were systematically investigated. The results highlight the critical role of multi-element doping and MWCNT integration in reducing the band gap and enhancing charge carrier dynamics. The presence of cerium significantly increased oxygen vacancies, while Ag nps contributed to improved visible light absorption through plasmonic resonance, and N doping further reduced the band gap. BET analysis confirmed a mesoporous structure that results in excellent degradation efficiencies of 87.5% for MB and 92.12% for CR in 80 minutes under visible-light irradiation. The synergistic effects of these modifications resulted in optimized ROS generation, leading to rapid degradation of organic dyes. Scavenger experiments confirmed that superoxide radicals ($^{\bullet}O_2^{-}$) and hydroxyl radicals ($^{\bullet}OH$) play dominant roles in the degradation of MB and CR dyes, as indicated by the significant reduction in degradation efficiency upon their quenching. Furthermore, reusability tests confirmed that the photocatalyst retained over 82% efficiency for MB and 87% for CR after four consecutive cycles, highlighting its stability and potential for repeated applications. The minor decline in performance was primarily attributed to material loss and partial pore blocking by dye intermediates. Thus, the synthesized photocatalyst is highly efficient for pollutant degradation.

Data availability

The data is available upon request.

Conflicts of interest

Authors have no conflict of interest.

Acknowledgements

We extend our gratitude to the Centre for Advanced Material Research and the Centre for IT and Automation at Kurukshetra University, as well as the RUSA Project Society (KURPS) under Rashtriya Uchchatar Shiksha Abhiyan (RUSA 2.0), for their generous funding and support towards this endeavor.

References

1 H. Kaur, *et al.*, Green synthesis of ZnO nanoparticles using E. cardamomum and zinc nitrate precursor: a dual-functional material for water purification and antibacterial applications, *RSC Adv.*, 2025, **15**, 16742–16765.
2 A. L. T. Zheng, C. A. C. Abdullah, E. L. T. Chung and Y. Andou, Recent progress in visible light-doped ZnO photocatalyst for pollution control, *Int. J. Environ. Sci. Technol.*, 2023, **20**, 5753–5772.
3 M. Mahajan, S. Kumar, J. Gaur, S. Kaushal, J. Dalal, G. Singh, M. Misra and D. S. Ahlawat, Green synthesis of ZnO nanoparticles using Justicia adhatoda for photocatalytic degradation of malachite green and reduction of 4-nitrophenol, *RSC Adv.*, 2025, **15**, 2958–2980.

4 S. Kumari, K. Sharma, S. Korpal, J. Dalal, A. Kumar, S. Kumar and S. Duhan, *et al.*, A comprehensive study on photocatalysis: materials and applications, *CrystEngComm*, 2024, **24**, 4886–4915.
5 I. H. Ifijen, M. Maliki and B. Anegbe, Synthesis, photocatalytic degradation and antibacterial properties of selenium or silver doped zinc oxide nanoparticles: a detailed review, *OpenNano*, 2022, **8**, 100082.
6 A. S. Chougale, S. S. Wagh, H. D. Shelke, S. F. Shaikh, R. D. Bulakhe, J. M. Kim, S. P. Patole and D. R. Shinde, Photocatalytic and antioxidant activity of ZnO/Cu/Ag/CNT nanocomposite, *J. Mater. Sci.: Mater. Electron.*, 2024, **35**, 990.
7 J. Dalal, *et al.*, *Nanomaterials: Synthesis and Applications*, Cambridge Scholars Publishing, 2024.
8 S. S. Wagh, A. S. Chougale, A. A. Survase, R. S. Patil, N. Naik, M. Naushad and H. M. Pathan, Rapid photocatalytic dye degradation, enhanced antibacterial and antifungal activities of silver stacked zinc oxide garnished on carbon nanotubes, *Sci. Rep.*, 2024, **14**, 14045.
9 A. K. Shimi, C. Parvathiraj, S. Kumari, J. Dalal, V. Kumar, S. M. Wabaidur and Z. Alothman, Green synthesis of SrO nanoparticles using leaf extract of Albizia julibrissin and its recyclable photocatalytic activity: an eco-friendly approach for treatment of industrial wastewater, *Environ. Sci. Adv.*, 2022, **1**, 849–861.
10 S. Rohilla, A. Gupta, V. Kumar, S. Kumari, M. Petru, N. Amor, M. T. Noman and J. Dalal, Excellent UV-light triggered photocatalytic performance of $ZnO{\cdot}SiO_2$ nanocomposite for water pollutant compound methyl orange dye, *Nanomaterials*, 2021, **11**, 2548.
11 S. Kumar, *et al.*, An Insight into Synthesis, Optical Properties, and Applications of Green Fluorescent Carbon Dots, *Crystals*, 2025, **15**, 320.
12 I. Ahmad, S. Shukrullah, M. Y. Naz, E. Ahmed, M. Ahmad, S. U. Rehman, H. N. Bhatti and A. Ghaffar, The role of synthesis method in hydrogen evolution activity of Ce doped ZnO/CNTs photocatalysts: a comparative study, *Int. J. Hydrogen Energy*, 2021, **46**, 30320–30333.
13 A. Murali, P. K. Sarswat and M. L. Free, Adsorption-coupled reduction mechanism in ZnO-Functionalized MWCNTs nanocomposite for Cr(VI) removal and improved anti-photocorrosion for photocatalytic reduction, *J. Alloys Compd.*, 2020, **843**, 155835.
14 M. Kumar, Supreet, S. Sharma, S. L. Goyal, S. Kumar, Asha, J. Dalal and R. Pal, Investigation of three-dimensional Mott's VRH conduction mechanism in core–shell structured polyaniline/zinc oxide nanocomposites for sensing applications, *Polym. Bull.*, 2025, **82**, 111–125.
15 A. Kumar, J. Dalal, S. Dahiya, R. Punia, K. D. Sharma, A. Ohlan and A. S. Maan, In situ decoration of silver nanoparticles on single-walled carbon nanotubes by microwave irradiation for enhanced and durable anti-bacterial finishing on cotton fabric, *Ceram. Int.*, 2019, **45**, 1011–1019.
16 P. M. Rajaitha, S. Hajra, M. Sahu, K. Mistewicz, B. Toroń, R. Abolhassani, S. Panda, Y. K. Mishra and H. J. Kim, Unraveling highly efficient nanomaterial photocatalyst for pollutant removal: a comprehensive review and future progress, *Mater. Today Chem.*, 2022, **23**, 100692.
17 S. Kumar, A. Kaur, J. Gaur, P. Singh, H. Kaur, S. Kaushal, J. Dalal and M. Misra, State-of-the-Art in Co_3O_4 Nanoparticle Synthesis and Applications: Toward a Sustainable Future, *ChemistrySelect*, 2025, **10**, e202405147.
18 F. M. Sanakousar, C. C. Vidyasagar, V. M. Jiménez-Pérez and K. Prakash, Recent progress on visible-light-driven metal and non-metal doped ZnO nanostructures for photocatalytic degradation of organic pollutants, *Mater. Sci. Semicond. Process.*, 2022, **140**, 106390.
19 N. Kadian, R. Kumari, A. Panchal, J. Dalal and D. Padalia, Structural and Optical Properties of Gadolinium Doped-Magnetite Nano-crystal for Photocatalytic Application, *J. Alloys Compd.*, 2023, **960**, 170811.
20 S. Ghaffar, A. Abbas, M. Naeem-ul-Hassan, N. Assad, M. Sher, S. Ullah, H. A. Alhazmi, A. Najmi, K. Zoghebi and M. Al Bratty, *et al.*, Improved photocatalytic and antioxidant activity of olive fruit extract-mediated ZnO nanoparticles, *Antioxidants*, 2023, **12**, 1201.
21 M. C. Uribe-López, M. C. Hidalgo-López, R. López-González, D. M. Frias-Márquez, G. Núñez-Nogueira, D. Hernández-Castillo and M. A. Alvarez-Lemus, Photocatalytic activity of ZnO nanoparticles and the role of the synthesis method on their physical and chemical properties, *J. Photochem. Photobiol., A*, 2021, **404**, 112866.
22 T. Saad Algarni, N. A. Y. Abduh, A. Al Kahtani and A. Aouissi, Photocatalytic degradation of some dyes under solar light irradiation using ZnO nanoparticles synthesized from Rosmarinus officinalis extract, *Green Chem. Lett. Rev.*, 2022, **15**, 460–473.
23 T. S. Aldeen, H. E. A. Mohamed and M. Maaza, ZnO nanoparticles prepared via a green synthesis approach: physical properties, photocatalytic and antibacterial activity, *J. Phys. Chem. Solids*, 2022, **160**, 110313.
24 P. Kumar, *et al.*, Recent advancements in pure and doped zinc oxide nanostructures for UV photodetectors application, *Phys. B*, 2025, **707**, 417177.
25 M. Samadi, H. A. Shivaee, M. Zanetti, A. Pourjavadi and A. Moshfegh, Visible light photocatalytic activity of novel MWCNT-doped ZnO electrospun nanofibers, *J. Mol. Catal. A: Chem.*, 2012, **359**, 42–48.
26 A. Kaur, S. Kumar, H. Kaur, G. S. Lotey, P. P. Singh, G. Singh, S. Kumar, J. Dalal, G. Bouzid and M. Misra, *et al.*, Enhanced photocatalytic degradation and antimicrobial activities of biogenic Co_3O_4 nanoparticles mediated by fenugreek: sustainable strategies, *Mater. Adv.*, 2024, **5**, 8111–8131.
27 S. Yadav, *et al.*, Facile synthesis of geopolymer composites for effectual removal of Cr(VI) and Cd(II) ions from aqueous solutions, *Discovery Mater.*, 2025, **5**, 1–18.
28 U. Wijesinghe, G. Thiripuranathar, H. Iqbal and F. Menaa, Biomimetic synthesis, characterization, and evaluation of fluorescence resonance energy transfer, photoluminescence, and photocatalytic activity of zinc oxide nanoparticles, *Sustainability*, 2021, **13**, 2004.

29 J. Gupta, P. A. Hassan and K. C. Barick, Structural, photoluminescence, and photocatalytic properties of Mn and Eu co-doped ZnO nanoparticles, *Mater. Today Proc.*, 2021, **42**, 926–931.

30 S. Kumari, *et al.*, Excellent photoelectrical properties of ZnO thin film based on ZnO/epoxy-resin ink for UV-light detectors, *AIP Conf.: Proc.*, 2019, **2142**, 120004.

31 T. V. H. Luu, M. D. Luu, N. N. Dao, V. T. Le, H. T. Nguyen and V. D. Doan, Immobilization of C/Ce-codoped ZnO nanoparticles on multi-walled carbon nanotubes for enhancing their photocatalytic activity, *J. Dispersion Sci. Technol.*, 2021, **42**, 1311–1322.

32 B. Amenu, A. M. Taddesse, T. Kebede, E. T. Mengesha and Z. Bezu, Polyaniline-supported MWCNTs/ZnO/Ag_2CO_3 composite with enhanced photocatalytic and antimicrobial applications, *Environ. Nanotechnol., Monit. Manage.*, 2024, **21**, 100926.

33 N. Mishra, S. Gulati, Y. Moriya, S. Kumar and G. Dubey, Enhanced photocatalytic degradation of hazardous dyes under visible light with biogenically synthesized ZnO-decked multi-walled carbon nanotubes (ZnO/MWCNT) nanocomposite: catalyst fabrication, performance and mechanistic insight, *Nano-Struct. Nano-Objects*, 2024, **39**, 101200.

34 J. Hou, L. Huang, Z. Yang, Y. Zhao, C. Deng, Y. Chen and X. Li, Adsorption of ammonium on biochar prepared from giant reed, *Environ. Sci. Pollut. Res.*, 2016, **23**, 19107–19115.

35 X. Ge, Z. Wu, Z. Wu, Y. Yan, G. Cravotto and B.-C. Ye, Microwave-assisted modification of activated carbon with ammonia for efficient pyrene adsorption, *J. Ind. Eng. Chem.*, 2016, **39**, 27–36.

36 T. Alammar and A.-V. Mudring, Facile preparation of Ag/ZnO nanoparticles via photoreduction, *J. Mater. Sci.*, 2009, **44**, 3218–3222.

37 D. Liu, Y. Liu, Z. Wu, F. Tian, B.-C. Ye and X. Chen, Enhancement of photodegradation of Ce, N, and P tri-doped TiO_2/AC by microwave radiation with visible light response for naphthalene, *J. Taiwan Inst. Chem. Eng.*, 2016, **68**, 506–513.

38 X. Wang, J. Song, J. Huang, J. Zhang, X. Wang, R. Ma, J. Wang and J. Zhao, Activated carbon-based magnetic TiO_2 photocatalyst codoped with iodine and nitrogen for organic pollution degradation, *Appl. Surf. Sci.*, 2016, **390**, 190–201.

39 X. Chen, Z. Wu, D. Liu and Z. Gao, Preparation of ZnO Photocatalyst for the Efficient and Rapid Photocatalytic Degradation of Azo Dyes, *Nanoscale Res. Lett.*, 2017, **12**, 4–13.

40 N. Huang, J. Shu, Z. Wang, M. Chen, C. Ren and W. Zhang, One-step pyrolytic synthesis of ZnO nanorods with enhanced photocatalytic activity and high photostability under visible light and UV light irradiation, *J. Alloys Compd.*, 2015, **648**, 919–929.

41 D. Jalandhara, S. Kumar, J. Dalal, G. Singh, S. Kumar, R. Badru, Y. Singh, S. V. Sharma and S. Kaushal, *et al.*, A multifunctional Co-doped $BiFeO_3$ nanocomposite: a promising candidate for photocatalytic degradation, antibacterial activity, and antioxidant applications, *Mater. Adv.*, 2025, **6**, 641–657.

42 X. Chen, Z. Wu, Z. Gao and B.-C. Ye, Effect of Different Activated Carbon as Carrier on the Photocatalytic Activity of Ag–N–ZnO Photocatalyst for Methyl Orange Degradation under Visible Light Irradiation, *Nanomaterials*, 2017, **7**, 258.

43 S. Sen Turkyilmaz, N. Guy and M. Ozacar, Photocatalytic efficiencies of Ni, Mn, Fe and Ag doped ZnO nanostructures synthesized by hydrothermal method: the synergistic/antagonistic effect between ZnO and metals, *J. Photochem. Photobiol., A*, 2017, **341**, 39–50.

44 R. R. Philip, U. P. Deshpande, V. A. Bunnell and N. M. Jobson, *et al.*, Cerium doped ZnO nanostructured photocatalyst for the degradation of multiple dyes, *J. Ind. Eng. Chem.*, 2024, **146**, 405–420.

45 J. Liu, J. Li, F. Wei, X. Zhao, Y. Su and X. Han, Ag–ZnO Submicrometer Rod Arrays for High-Efficiency Photocatalytic Degradation of Congo Red and Disinfection, *ACS Sustainable Chem. Eng.*, 2019, **7**, 11258–11266.

46 D. G. Ayu, S. Gea, Andriayani, D. J. Telaumbanua, A. F. R. Piliang, M. Harahap, Z. Yen, R. Goei and A. I. Y. Tok, Photocatalytic degradation of methylene blue using N-doped ZnO/carbon dot (N-ZnO/CD) nanocomposites derived from organic soybean, *ACS Omega*, 2023, **8**, 14965–14984.

47 N. Chauhan, V. Singh, S. Kumar, K. Sirohi and S. Siwatch, Synthesis of nitrogen-and cobalt-doped rod-like mesoporous ZnO nanostructures to study their photocatalytic activity, *J. Sol-Gel Sci. Technol.*, 2019, **91**, 567–577.

48 V. S. Kundu, N. Chauhan and S. Kumar, Enhanced photocatalytic and disinfection activities of silver loaded ordered mesoporous titanium dioxide for water treatment, *Indian J. Pure Appl. Phys.*, 2017, **55**, 881–889.

49 A. Dhanalakshmi, B. Natarajan, V. Ramadas, A. Palanimurugan and S. Thanikaikarasan, Structural, morphological, optical and antibacterial activity of rod-shaped zinc oxide and manganese-doped zinc oxide nanoparticles, *Pramana*, 2016, **87**, 1–9.

50 M. Kumari, V. S. Kundu, S. Kumar, S. Siwatch and N. Chauhan, Nitrogen and silver codoped one-dimensional ZnO nanostructure for optoelectronic application, *J. Sol-Gel Sci. Technol.*, 2020, **93**, 302–308.

51 N. Chauhan, V. Singh, S. Kumar and R. L. Dhiman, Influence of nickel, silver, and sulphur doping on the photocatalytic efficiency of mesoporous ZnO nanoparticles, *Arabian J. Sci. Eng.*, 2020, **45**, 249–259.

52 M. Singh, P. Kumar, N. Singh and A. Jain, Microwave irradiation synthesis of nitrogen doped Ag/MWCNT/ZnO nanocomposite for photocatalytic application, *Rasayan J. Chem.*, 2023, **16**, 268–275.

53 M. Dagar, S. Kumar, A. Jain and M. Singh, Sucheta, Advanced Synthesis and Bandgap Engineering of Ag/Ce/N/ZnO Ternary Nanocomposites for Enhanced Photodegradation of Organic Dyes, *Powder Metall. Met. Ceram.*, 2025, 1–14.